PCCP

RSC Publishing

PAPER

View Article Online
View Journal | View Issue

New insight into the discharge mechanism of silicon–air batteries using electrochemical impedance spectroscopy†

Cite this: *Phys. Chem. Chem. Phys.*, 2013, **15**, 3256

Gil Cohn,[a] Rüdiger A. Eichel[b] and Yair Ein-Eli*[a]

Received 1st November 2012,
Accepted 4th January 2013

DOI: 10.1039/c2cp43870d

www.rsc.org/pccp

The mechanism of discharge termination in silicon–air batteries, employing a silicon wafer anode, a room-temperature fluorohydrogenate ionic liquid electrolyte and an air cathode membrane, is investigated using a wide range of tools. EIS studies indicate that the interfacial impedance between the electrolyte and the silicon wafer increases upon continuous discharge. In addition, it is shown that the impedance of the air cathode–electrolyte interface is several orders of magnitude lower than that of the anode. Equivalent circuit fitting parameters indicate the difference in the anode–electrolyte interface characteristics for different types of silicon wafers. Evolution of porous silicon surfaces at the anode and their properties, by means of estimated circuit parameters, is also presented. Moreover, it is found that the silicon anode potential has the highest negative impact on the battery discharge voltage, while the air cathode potential is actually stable and invariable along the whole discharge period. The discharge capacity of the battery can be increased significantly by mechanically replacing the silicon anode.

1. Introduction

Developing new alternative sources for energy generation and storage is a key issue these days and a growing global concern. Lithium-based battery systems, such as Li–ion and Li–oxygen, have drawn much attention, due to their high energy density. However, the increased demand for Li–ion batteries from the portable electronics and the massive introduction of Li batteries to the electric vehicles market pose a major problem of Li abundance, price and geographical reserve.[1,2]

Recently, much of the research attention has been focusing on metal–air batteries. The active reactants in metal–air cells are metal anodes and oxygen (from ambient air or from O_2 reservoir). Oxygen is reduced on an air cathode, mostly a carbon electrode having a porous structure, which acts as a gas transport medium to the solid–electrolyte interface.[3–5] The carbon is supported by an oxygen reduction reaction (ORR) catalyst, catalysts with many types of noble as well as non-noble metals, metal oxides and nitrogen alloys have been investigated over the past few years.[6–14] Oxygen is not stored in the battery pack; hence, both theoretical specific energy and theoretical energy density are extremely high for metal–air systems.

Of the different types of metal–air batteries, metals such as Al, Fe, Mg, Zn and Li are most common and appropriate to serve as anodes. The primary aqueous Zn–air cell has long been commercialized as the energy source for hearing aids.[15,16] Electrically rechargeable metal–air systems are still in the research stage. The most studied rechargeable system is Li–air, first introduced by Abraham and Jiang in 1996.[17] The theoretical specific energy excluding oxygen is nearly 11 200 W h kg^{-1}, very close to that of the dense gasoline systems. However, Li–air still suffers from major problems, mainly low cycling efficiency and very limited reaction kinetics at the air cathode, which forces low operation electrical currents.[18–20]

Silicon as an interesting alternative to the conventional anode metals has been introduced by our research group.[21,22] In terms of theoretical gravimetric energy density, silicon exhibits a favorable value of 8470 W h kg^{-1}, compared to Al, Mg and Zn anodes. Moreover, silicon is the second most abundant element of the earth's crust, and as such, no shortage in Si supply is expected at any time. The Si–air, employing 1-ethyl-3-methylimidazolium oligofluorohydrogenate (EMI·$(HF)_{2.3}$F), a room temperature ionic liquid (RTIL) electrolyte, and an n-type heavily doped Si wafer as the anodic fuel, exhibits typical discharge

[a] *Department of Materials Science and Engineering, Technion - Israel Institute of Technology, Haifa 32000, Israel. E-mail: eineli@tx.technion.ac.il*
[b] *Forschungszentrum Jülich, Institut für Energie und Klimaforschung IEK-9, Jülich 52425, Germany*

† Electronic supplementary information (ESI) available. See DOI: 10.1039/c2cp43870d

potentials of 0.8–1.1 V. In a recent paper it was shown that the addition of water to the ionic liquid electrolyte results in higher ionic conductivity and higher discharge capacities.[23] This behavior was attributed to a shift in the reaction zone for discharge products from the surface of the air cathode into the bulk electrolyte. The discharge products, mostly SiO_2, are believed to be deposited on the air cathode and therefore responsible for discharge failure. It was reported that a generation of discharge products away from the air cathode surface is responsible for postponed suffocation of pores in the air cathode.

In a most recent study, the role of an ORR catalyst in the performance of Si–air was studied.[24] This report examines the chemical state of Mn ions in the MnO_2 catalysts by means of X-ray photoelectron spectroscopy (XPS) and electron paramagnetic resonance (EPR) spectroscopy. The results suggest that along the discharge process, MnO_2 suffers from an electrochemical reaction with the fluoride containing electrolyte ions. The reaction involves transformation of MnO_2 to the non-ORR catalyst MnF_2. Such reaction causes loss of available catalytic sites, lowered ionic conductivity of the electrolyte, and solids volume expansion in the pores orifice.

The present study is focused on the elucidation of fundamental insight into the generation and development of silicon and air cathode interfaces in the battery during storage and operation, and the roles of the evolved interface in the battery's failure mechanism. For this purpose, electrochemical impedance spectroscopy (EIS) is primarily being utilized. EIS is one of the strongest electrochemical tools for analyzing the evolution of such interfacial reactions. The EIS technique permits differentiation and comparison between interfacial reactions, as well as different surface interactions. In this framework, we describe the impedance behavior of an Si–air cell, emphasizing the silicon anode, at different depths of discharge. We discuss the contributions of silicon interface resistance and porous structure evolution to the total impedance, as well as the different behavior of various silicon types. A three-electrode configuration is also used to differentiate between the potential contributions of each electrode in the battery.

2. Experimental

The air cathode (Electric Fuel, Israel) was constructed from a mixture of activated carbon black and polytetrafluoroethylene (PTFE) binder, catalyzed by MnO_2, onto an Ni grid. Silicon anodes were cut from {100} oriented Si wafers: n-type As-doped 0.001–0.005 Ω cm (University Wafers, USA, further referred to as n^{++}), n-type As-doped 0.1–0.6 Ω cm (University Wafers, USA, further referred to as n^{+}), and p-type B-doped 0.001–0.005 Ω cm (Si-Mat, Germany, further referred to as p^{++}). All silicon samples were cleaved to approximate 1 cm × 1 cm pieces, with the exposed surface controlled by an O-ring. Samples were cleaned in 1 : 1 H_2SO_4 : H_2O_2 solution to remove organic contaminations and washed with DI water. Afterwards the samples were dipped in 20 vol% HF solution in order to remove native oxide, then washed with DI water again and dried with a N_2 stream.

For electrochemical measurements a Si–air cell was incorporated as described in a previous paper,[22] with a commercial electrolyte solution of EMI·$(HF)_{2.3}$F RTIL (Boulder Ionics, USA). The cells were assembled and operated in an ambient atmosphere. A three-electrode half-cell was fabricated out of a Si wafer or an air cathode working electrode, Pt wire as a counter electrode and a home-built gelled reference electrode. More details about the reference electrode preparation procedure and testing can be found in ref. 25.

The electrochemical evaluations of the battery configuration were performed at room temperature with an Arbin BT-2000 battery tester. The cells were kept in an open circuit condition for 4 hours prior to operation, in order to assure proper wetting of the porous air cathode by the electrolyte. For EIS measurements, an AC amplitude of 5 mV was applied, with zero DC voltage bias, over a frequency range of 1 MHz to 10 mHz. All half-cell electrochemical tests and EIS measurements were carried out using a 2273 EG&G Princeton Applied Research potentiostat/galvanostat. The measured impedance data were analyzed and fitted to an equivalent circuit model by nonlinear least square fitting software (ZSimpWin, EChem software).

All EIS results were obtained with n-type and p-type silicon substrates in the dark to avoid minority charge carrier generation by illumination. Ohmic contacts were obtained by applying Ag paste on the back sides of the samples.

3. Results and discussion

Silicon–air batteries consist of, in addition to the already complex solid electrodes (silicon anode and air membrane cathode), several complicated interfaces, such as the porous carbon air cathode–RTIL electrolyte, and RTIL electrolyte–silicon anode wafers. The relative magnitude of the measured impedance of each element can provide an insight into the local discharge mechanism. The EIS spectra (presented as Nyquist plots), for a Si–air battery tested with an n^{++} silicon anode, measured in different points throughout the discharge process, are shown in Fig. 1. The impedance

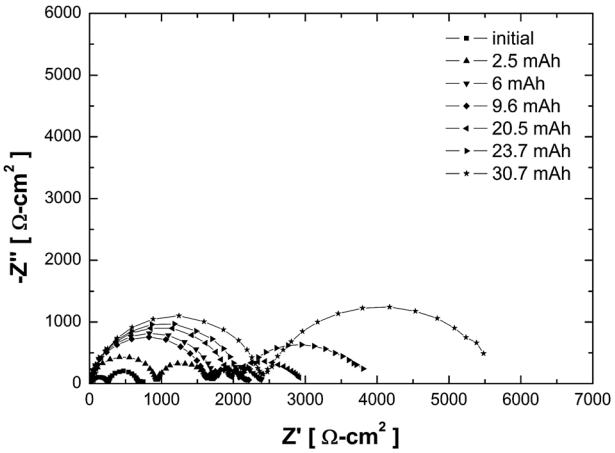

Fig. 1 Nyquist plots for Si–air cell, utilizing n^{++} silicon anode and air cathode, with EMI·$(HF)_{2.3}$F electrolyte. Impedance spectra were taken along discharge at a current density of 0.3 mA cm^{-2}.

response is characterized by two well-defined flattened semicircles, separated into high- and low-frequency regions. The plots in Fig. 1 present an insight into the overall interfacial phenomenon occurring at both electrodes. However, in order to specifically determine which electrode is the most dominant source, contributing to the cell impedance, one needs to analyze the interfacial phenomenon of a single electrode, either the silicon anode or the air cathode membrane. Thus, it is necessary to obtain and analyze the impedance spectra of each electrode. The impedance spectra of the silicon half-cell and the air cathode half-cell are shown in Fig. 2. These two spectra are clearly very different in their shape, indicating two well-diverse processes. The spectra in Fig. 2 were obtained at open circuit potential (OCP) and at a discharge depth of 6.4 mAh, while similar results were obtained at different discharge capacities. The plot for the silicon anode presented in Fig. 2 exhibits almost an identical shape of two large semicircles as the impedance plot obtained from the battery, shown in Fig. 1. On the other hand, the total impedance

$$Z_{\text{tot}} = \sqrt{|Z'|^2 + |Z''|^2} \quad (1)$$

of the air cathode is significantly lower than the one measured at the anode, and thus it can be neglected. It is noteworthy that the cathode spectrum also includes an inductive part in the high frequency range. This inductance element was already observed in several studies, and was ascribed to carbon electrode geometry and to electrical wiring problems.[26,27]

Nevertheless, from the comparison between single electrode EIS results presented in Fig. 2 and the total battery spectra shown in Fig. 1, it can be concluded that the major source of Si–air battery impedance originates from the Si anode, while the air cathode has only insignificant contribution. This is in contrast to other metal–air batteries, especially Li–air, where the carbonaceous air cathode (porous or layered carbon) is the dominant impedance factor and its over-potential governs the discharge performance.[28,29] Moreover, modifications in the Li–air battery air cathode porosity, material composition and oxygen pressure greatly affect the values of impedance components and the shape of impedance spectra.[29–31]

Using the impedance results of the single electrode, the silicon anode or the air cathode, as reference data, it is now possible to analyze the spectrum of the complete Si–air battery. Although this spectrum contains a combination of the two electrodes spectrum, due to the neglected impedance of the air cathode all the significant processes, from an impedance measurement point of view, are actually occurring at the anode solely. The intercept with the real axis at high frequency is the sum of uncompensated electrolyte, semiconductor bulk and contact resistances, such as the electronic resistance of the current collectors. The high frequency semicircle can be attributed to a charge transfer resistance and a space charge layer capacitance. The second semicircle, at low frequencies, is accounted for the resistance and capacitance of the sub-micron pores, covered with a thin oxide layer, that are being formed during anodic reaction on the silicon wafer.[22,32,33]

The different impedance components of the battery can be further analyzed by means of fitting an electrical equivalent circuit. Fig. 3a shows an appropriate electrical description of the battery impedance structure, in terms of an equivalent circuit. The circuit consists of a resistance element connected in series to an RC element, which is connected in parallel to another RC component. This circuit is based on the model suggested by Shen *et al.*[34] for a macroporous silicon substrate, in which the space-charge layer is located at the bottom of the pores. Our suggested circuit includes a modification to the model in ref. 34, in order to apply it for sub-micron pores. The circuit elements are as follows: R_b – solution resistance together with external ohmic resistance, R_{ct} – charge transfer resistance, and Q_{sc} – constant phase element (CPE), represents space charge layer capacitance. R_p and Q_p are the resistance and CPE, respectively, attributed to the porous layer. Fig. 3b presents a schematic description of a porous silicon structure,

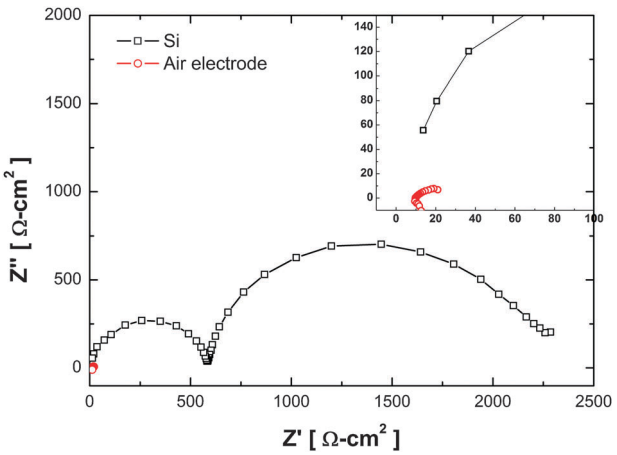

Fig. 2 Nyquist plots for Si anode and air cathode half cells. Inset shows inductive behavior for air cathode under high frequencies.

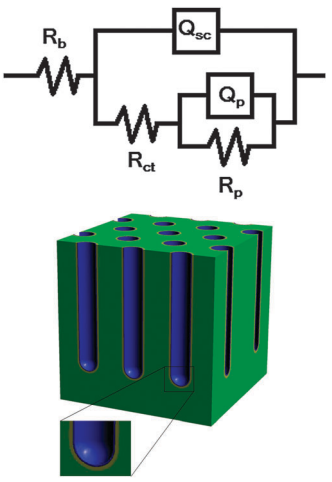

Fig. 3 (a) Equivalent circuit chosen to model the impedance behavior of an Si–air battery. (b) Schematics of porous anode surface. Inset exhibits two surface layers; the inner represents the space charge layer and the outer represents the oxide layer.

elucidating the suggested equivalent circuit. It should be noted that CPE elements were needed to replace ideal capacitance elements in order to get a better matching to the measured data. Due to the rough (porous) surface of the silicon anode, the usage of pure capacitance element, based on parallel plates, is not acceptable. The impedance of a CPE is expressed by

$$Z_{\mathrm{CPE}}(\omega) = \frac{1}{(i\omega)^n \tilde{C}} \quad (2)$$

The unit of $\tilde{C}$, the pseudocapacity term, is $s^n/(\Omega\ cm^2)$. The power n depends on the porosity of the electrode and expresses the deviation from an ideal capacitor. A value of $n = 1$ represents the pure capacitance element. ω is the angular frequency.

As mentioned before, the contribution of the air cathode to the total impedance of the cell is neglected. Accordingly, the EIS data give no indication for a diffusion controlled process, being a common element, when describing an equivalent circuit for an air cathode.[30,35] Due to the high signature of silicon impedance, all impedance marks of diffusion processes that take place on the air cathode membrane are masked by the processes on the anode. Consequently, the proposed model does not contain any diffusion element.

Using ZSimpWin V3.22 software (EChem Software), the equivalent circuit was fitted to the experimental spectra, and the equivalent circuit parameters were quantitatively obtained, as listed in Table 1. The calculated parameters are normalized by the nominal surface area and not by the real exposed area. The initial electrolyte resistance (R_b @ fresh condition) was found to be 5.7 $\Omega\ cm^2$. This value is in very good agreement with the electrolyte conductivity, 100 mS cm^{-1}, when taking into account the distance of 9 mm between the cathode and the anode in the battery cell and the exposed surface area of 0.5 cm^2. However, from Table 1 it can be seen that the electrolyte resistance increases with an increase in discharge length (capacity). This can be due to reduced electrolyte conductivity inside the formed pores at the silicon surface, as well as to the contribution of SiF_4 formation at the anode during discharge. The formation of SiF_4 can also provide an explanation for the increase in R_{ct} with discharge time.

Table 1 shows that the value of $\tilde{C}_{sc}$ does not change much with discharge time, and fluctuates around the value of $7 \times 10^{-9}\ s^n/(\Omega\ cm^2)$. The steady value of $\tilde{C}_{sc}$ suggests that the area of the space-charge layer does not change significantly along discharge, although the continuous formation of the porous layer is observed. This finding indicates that the charge transfer process occurs only at the bottom of the pores, or on the outer flat surface, and not on walls of the pores. The values of the exponential factor n_{sc} in Table 1 strengthen the above-mentioned assumption. This parameter keeps a constant value, very close to 1, along the discharge process, indicating a good capacitor character of this CPE. From $n_{sc} \approx 1$ one can deduce that the space charge region is very much flattened, *i.e.* parallel plate capacitance, again indicating reaction only through the pores base and through the outer flat surface.

As pointed out in the previous discussion, the magnitude of $\tilde{C}_{sc}$ is kept almost constant along the discharge process. This behavior indicates that the electrode kinetics, controlled by a space charge layer, is constant during discharge. The electrode kinetics in this case is determined by the rate of electron generation at the n-type semiconductor conduction band, due to its band bending under anodic polarization.[36,37] A support to this assumption can be found in Fig. 4, showing a comparison between Q_{sc} values obtained from medium doped (n^+) and heavily doped (n^{++}) n-type silicon wafers. The changes in Q_{sc} shown in Fig. 4 were recorded using a symmetric test cell, with Si wafers serving as both working and counter electrodes. This structure is useful when one desires to investigate the properties of only one of the electrodes, as the only interface in the system is the one between the electrolyte and the single electrode. The EIS measurements in Fig. 4 were taken at OCP and along a continuous storage at OCP, as well. As expected, the impedance spectra obtained both for n^+ and n^{++} silicon exhibit two semicircles (not shown), similar in shape to the plots presented in Fig. 1. In order to compare the magnitude of capacitance between the two different samples we cannot rely on the values of $\tilde{C}_{sc}$ solely since the dimension of $\tilde{C}_{sc}$, $s^n/(\Omega\ cm^2)$ depends on the value of the exponential factor n, whereas n value changes from one measurement to another. Therefore, a conversion must be made from $\tilde{C}_{sc}$ experimental pseudo-capacitance to comparable "real" capacitance values, C_{sc}. This can be achieved using the method suggested by Hsu and Mansfeld.[38] According to their procedure, the conversion of $\tilde{C}_{sc}$ to C_{sc} is performed by applying the following equation:

$$C_{sc} = \tilde{C}_{sc}\ (\omega_m)^{n-1} \quad (3)$$

where ω_m is the frequency at which Z'', the imaginary part of the impedance, reaches its maximum value. Using eqn (3), the space charge capacitances of n^+ and n^{++} samples were calculated. Values of ω_m were extracted from Bode plots utilizing the impedance imaginary part *vs.* the frequency (See Fig. S1 in ESI†). The numerical results of Q_{sc} (n_{sc} in Fig. 4b and C_{sc} in Fig. 4c),

Table 1 Parameters of equivalent circuit for different periods along discharge

	Fresh	Q = 2.5 mAh	Q = 6 mAh	Q = 9.6 mAh	Q = 20.5 mAh	Q = 23.7 mAh	Q = 30.65 mAh
$R_b/\Omega\ cm^2$	5.71	6.52	7.78	10.66	22.37	29.74	66.68
Q_{sc} ($\tilde{C}$)/nS $s^n\ cm^{-2}$	33.7	7.08	6.95	6.75	7.42	7.70	6.48
Q_{sc} (n)	0.918	0.986	0.985	0.988	0.978	0.974	0.988
$R_{ct}/\Omega\ cm^2$	251.3	911.2	1719	1572	1898	2032	2289
Q_p ($\tilde{C}$)/μS $s^n\ cm^{-2}$	13.2	14.9	21.3	24	33	41.1	33.2
Q_p (n)	0.956	0.875	0.817	0.793	0.773	0.786	0.785
$R_p/\Omega\ cm^2$	426.6	775.4	657.6	610.2	1025	1786	3440

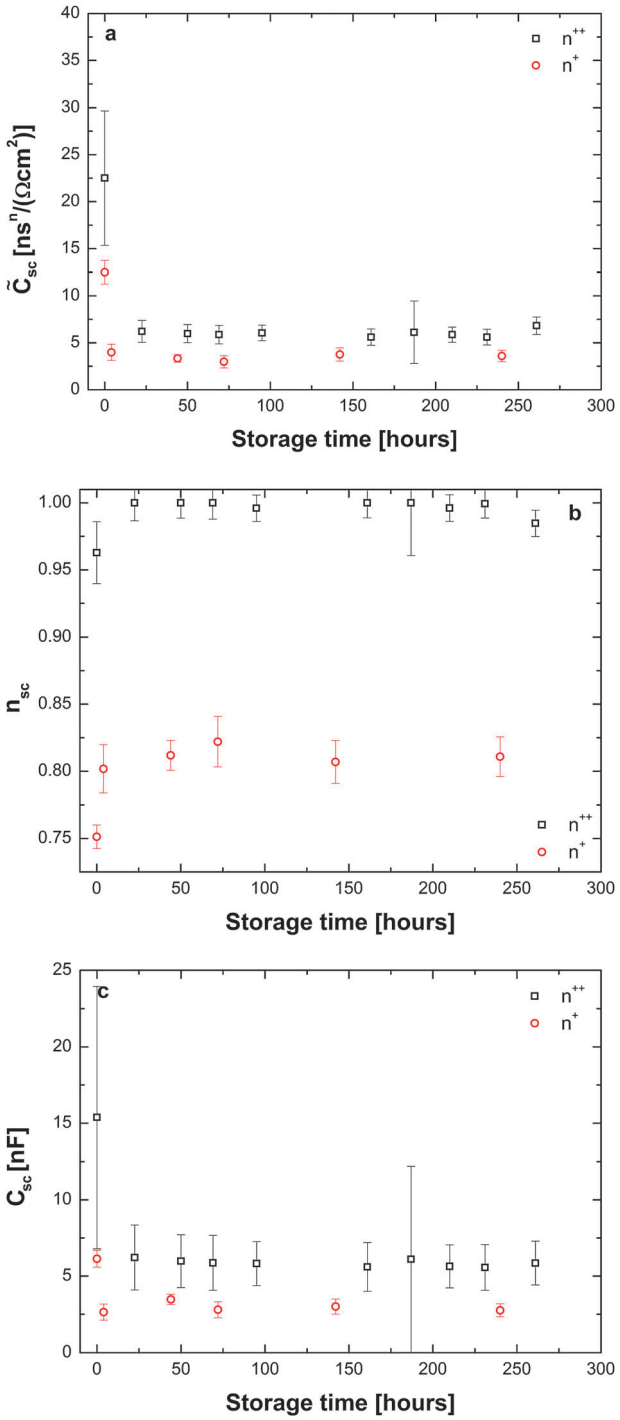

Fig. 4 Time dependence of (a) $\tilde{C}_{sc}$, (b) n_{sc}, and (c) C_{sc} by fitting EIS measurements of n^+ and n^{++} silicon anodes at OCP.

accounting for the capacitance contribution of the space charge layer in the semiconductor, show dependence on the doping level and are smaller for the n^+ silicon than for the n^{++} silicon wafer. The potential profile across the interface between the silicon electrode and the electrolyte is distributed between the space charge layer, which depends on the doping level, and the Helmholtz layer, being considered as constant. Therefore, this difference in the value of C_{sc} indicates that the number of charge carriers in the semiconductor depletion layer is higher for n^{++} silicon. This means that higher doping levels in the silicon gives rise to increased (pseudo-) capacitance values, and that the potential drop, followed by band bending, is steeper. These results are in agreement with the potentiodynamic observations presented in ref. 21, which show much smaller anodic current density for n^+ than for n^{++} silicon wafers. The current flows across the electrode–electrolyte interface is governed, among other factors, by the drop of potential in the space charge region, with steeper drop leads to higher currents. From the value of the exponential factor n_{sc} presented in Fig. 4b, it can be seen that the capacitance component Q_{sc} shows much lesser ideal capacitor behavior in the n^+ silicon wafer compared with the same component for n^{++} silicon.

The impedance of the porous layer, Q_p CPE presented in Table 1, behaves however much differently than Q_{sc}. The value $\tilde{C}_p$ shows a slight increase, while the deviation of n_p from unity increases significantly with discharge time. The value of n_p starts from 0.95, and reaches 0.78 at the end of the discharge process. This indicates that the discharge process causes advanced deviation from ideal RC behavior. Together with the increase in R_p, this behavior can be associated with the formation and on-going growth of the porous layer at the anode surface with the application of anodic polarization (discharge). Along with the advance in pores depth into the anode, a passivation layer is being formed along the pore walls, which contributes to the observed increase in R_p. The formation of the oxide layer together with porous structure is responsible for increased charge storage in this film, leading to a higher value of $\tilde{C}_p$ with respect to $\tilde{C}_{sc}$.[39]

Values for the porous layer capacity C_p were evaluated with the same method as for C_{sc}, using eqn (3). These values were calculated for two distinguished cases – throughout the discharge process and during storage at OCP. The results, shown in Fig. 5, suggest that even though we cannot treat the

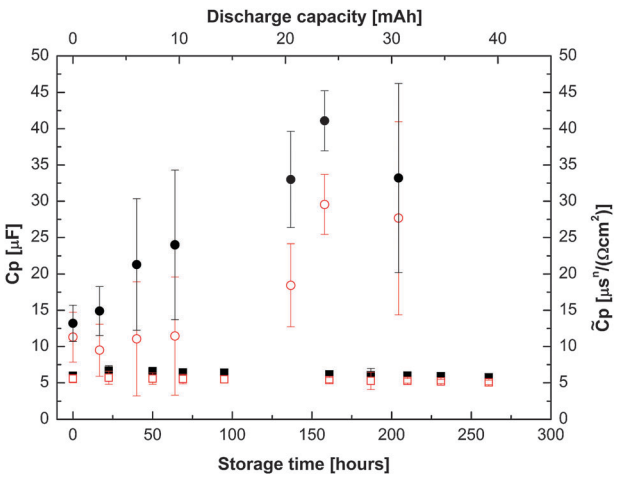

Fig. 5 Variation of $\tilde{C}_p$ (solid symbols) and C_p (empty symbols) as a function of storage time (square) and discharge capacity (circle). $\tilde{C}_p$ and C_p values were obtained by fitting EIS measurements of n^{++} silicon anodes.

pseudo-capacity as the "real" capacity, the trend is very much similar for both terms. Another important result, as shown in Fig. 5, is that when considering the difference in porous layer capacitance between the "rest" and the "working" samples, there is a large difference between the two. While in "rest", C_p (and $\tilde{C}_p$) keeps its value constant, under a discharge procedure the value for C_p (and $\tilde{C}_p$) is growing with time (discharge length). These results serve as evidence that not only a porous layer is being formed at the silicon anode surface under anodic polarization (discharge), but also that the porous layer thickness is increasing with time,[33] leading to a higher surface area and hence, increased capacity.

In previous works[23,24] it was found that there are two major factors contributing to Si–air discharge termination: formation of reaction products in the air electrode during cell discharge, and the conversion of the MnO_2 ORR catalyst to the non-ORR catalyst MnF_2. Accordingly, it is logical to focus the research on finding ways to improve the efficiency of the air cathode for ORR in Si–air batteries. However, as discussed previously, the results in this paper show that the silicon anode, and not the cathode, is the dominant segment contributing to the majority of the cell impedance. Therefore, it is likely to assume that failure in battery operation would first be originated from the silicon anode inactivation mechanism, while the air cathode is still available for reduction of oxygen. In order to identify the role of silicon in the potential drop of the battery during discharge, we employed a three-electrode configuration to the Si–air system. The potential of the Si anode and the air cathode was recorded separately during discharge using a reference electrode, while the battery voltage was recorded simultaneously as well. This was performed with Si–air cells utilizing n^+, n^{++} and p^{++} silicon wafers. The graphs shown in Fig. 6 present the absolute change in a single electrode potential with respect to its initial potential,

$$\Delta V(t) = |V(t) - V(t = 0)| \quad (4)$$

This graphical representation is more suitable when exploring the over-potential, or potential drop, at an electrode. As shown in Fig. 6, it is clear that the initial drop in electrode potential, or activation polarization, is much larger for the air cathode than for the silicon anode. This observation is well applied in all investigated types of silicons. The decrease in the air cathode potential at the early stages of discharge is attributed to the consumption of dissolved oxygen near the electrode surface or the consumption of pre-absorbed oxygen at the carbon air membrane material. Since these oxygen molecules are easy to be accessed, the initial potential is high, however it drops when more and more oxygen is being consumed and reduced. Nevertheless, after this first step of potential decline, the air electrode potential keeps a steady trend, with a ΔV value of around 0.5 V, regardless of the silicon type being used. Moreover, the plateau period observed at the air cathode is being reached after an equivalent discharge capacity of $\sim$2 mAh, again without any correlation with the type of silicon being used. These findings support our assumption that the initial decrease in the potential of the air cathode, equivalent to

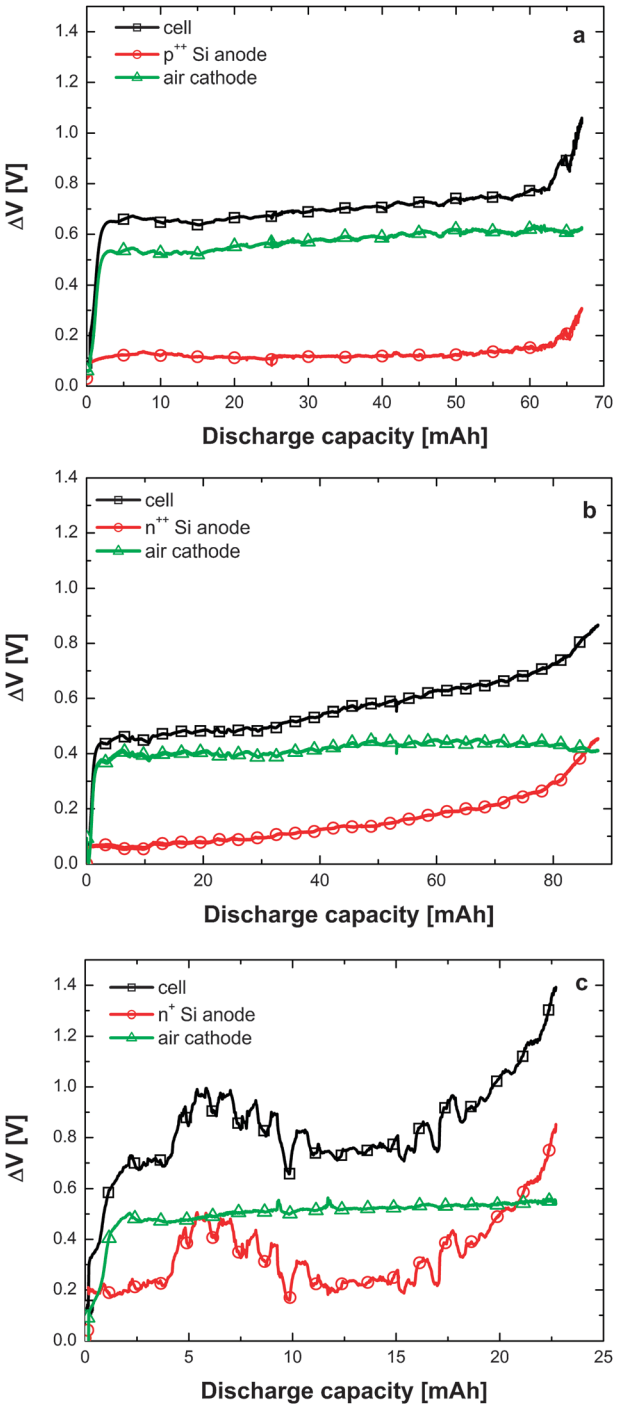

Fig. 6 Potential drop of Si–air cell, silicon anode and air cathode membrane, recorded with 3 – electrode Si–air cell, using (a) p^{++}, (b) n^{++}, and (c) n^+ silicon wafers. Discharge current density 0.3 mA cm^{-2} for p^{++} and n^{++}, 0.1 mA cm^{-2} for n^+.

gradual over-voltage, is due to a rather easier oxygen diffusion and consumption near the electrode–electrolyte interface.

The silicon anode, on the other hand, behaves much differently upon discharge than the air cathode. First, Fig. 6 shows that the primary voltage drop at the silicon anode is only 0.1 V for p^{++} (a), 0.2 V for n^{++} (b) and 0.4 V for n^+ (c). These findings agree well with previous studies of the potentiodynamic

behavior of silicon wafers in EMI·$(HF)_{2.3}F$ ionic liquid, which showed large over-potential under anodic polarization for n^+ compared to n^{++} and p^{++}.[22] Second, it can be seen that the curves for a silicon anode and a complete cell are almost identical, once the air cathode potential acquires its constant value. This strong similarity is most importantly seen at the end of discharge, where the over-potential of the silicon electrode shows a steep incline, causing an equivalent decrease in the cell voltage until failure. The most important conclusion from Fig. 6 is that for both n- and p-type silicon anodes, the voltage profile of the Si–air battery mimics the anode profile, while the voltage of the air cathode remains almost unmodified. The results in Fig. 6 confirm the assumption that the silicon anode is indeed the dominant electrode which controls and defines the discharge behavior of the Si–air system, and determines its working voltage, as well as its capacity. Although silicon oxide discharge products do accumulate at the air cathode,[22,23] this deposit layer does not govern the total discharge capacity. In Li–air batteries however, many studies have shown that the opposite occurs, as Li oxides and carbonate products prevent continuous operation of the air electrode due to oxygen diffusion blocking.[18–20,41] Moreover, these studies show that the over-potential at the air cathode side is the major contributor to the Li–air over-potential, during both discharge and charge processes. Therefore, many of the recent Li–air studies focus on improvements of the air cathode and on developing new materials for the cathode.[40,42–44] In Si–air battery technology, however, this is not the case, and it actually seems to be the opposite – the discharge potential of the battery is governed mainly by the potential of the anode.

Another observation on the importance of the silicon anode with respect to the discharge of the Si–air cell can be found in Fig. 7, which compares the performance of two identical Si–air cells being discharged at a constant current density. However, during the discharge of the cells, and also after the end of discharge, one of the electrodes was replaced with a fresh one; silicon anode (shown in Fig. 7a) and air cathode membrane (shown in Fig. 7b). As indicated in Fig. 7, replacement of the anode in the middle of discharge (first exchange in Fig. 7a) does not affect the discharge voltage. However, the discharge capacity obtained at the end of operation of the second silicon anode is increased and almost doubled compared to a complete single discharge with a single anode.[22] Nevertheless, every substitution of the silicon wafer does not correspond with equivalent capacity for each silicon anode being replaced. As the discharge process is extended, the capacity of each changing period is decreased significantly to such an extent that at the fifth replacement the delivered discharge capacity is negligible compared to the capacity recorded with the first silicon electrode being utilized. These results indicate that although the performance of the Si–air battery is indeed anode limited, the air membrane and the electrolyte degrade during the discharge process as well. We can assume that the resistivity of the ionic liquid electrolyte probably increases, while the air cathode is blocked by discharge products. On the air membrane cathode issue: the same procedure of electrode

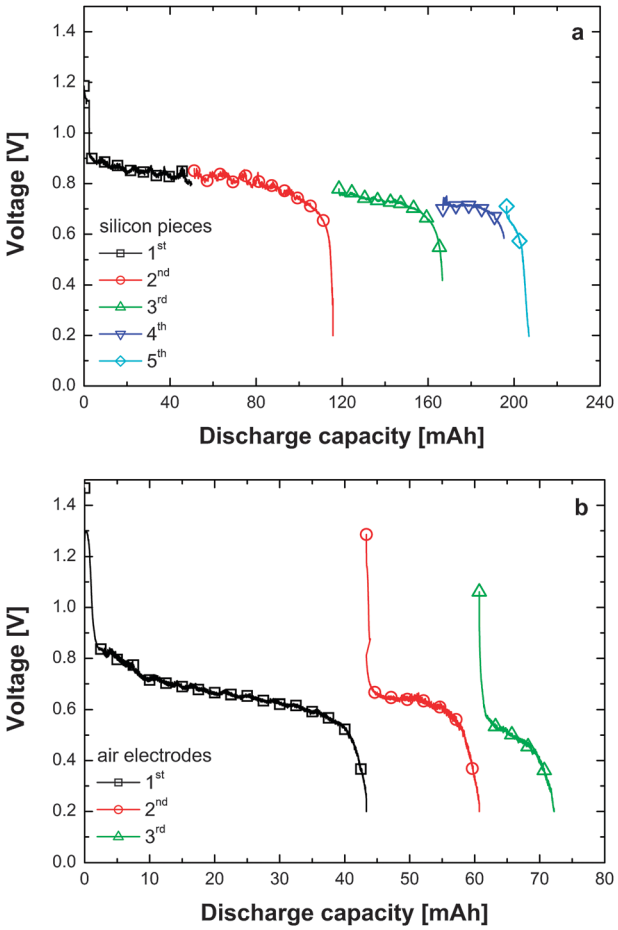

Fig. 7 Discharge curves of Si–air cell at a current density of 0.3 mA cm^{-2}, while exchanging the (a) silicon anode, (b) air cathode during discharge.

refreshing during discharge was conducted for the air cathode membrane, as shown in Fig. 7b. It can be seen that substitution of the air cathode after the end of discharge does extend the discharge capacity, but in a much smaller value compared with the capacity extension due to silicon anode replacement.

4. Conclusions

In summary, we present the results of systematic electrochemical studies describing the discharge profile of an Si–air battery. EIS recorded along a discharge process was used to characterize the interfaces between the batteries' electrodes and the electrolyte. EIS results show negligible impedance contribution of the processes at the air cathode compared to the silicon anode. Analyzing the impedance data in terms of the electrical equivalent circuit reveals the parameters related to space charge capacitance and charge transfer, and indicates that the active electrochemical area remains unchanged, even though the formation of porous structure is observed. Furthermore, the capacitance of the space charge layer is well correlated to the doping type and concentration of the silicon anode. Comparing the potential profile of the complete Si–air cell to that of the distinctly two electrodes provides experimental evidence for

the domination and the most negative impact (in terms of capacity and voltage drop of the Si–air cell) of the silicon anode over the air cathode. The discharge capacity of Si–air batteries can be significantly increased by replacing the discharged inactivated silicon anode towards the end of the discharge process. These findings provide a viable rationale for the development of a mechanically rechargeable design for Si–air batteries, where the batteries' mode of operation would be solely in a discharge mode, and thus there is no need for bi-functional air electrodes.

Acknowledgements

This work was supported by the G.I.F research grant G-1041-71.5/2009, by Grand Technion Energy Program (GTEP) and Helmsley Charity Funds.

References

1 C. Grosjean, P. H. Miranda, M. Perrin and P. Poggi, *Renewable Sustainable Energy Rev.*, 2012, **16**, 1735–1744.
2 S. H. Mohr, G. Mudd and D. Giurco, *Minerals*, 2012, **2**, 65–84.
3 F. Bidault, D. J. L. Brett, P. H. Middleton and N. P. Brandon, *J. Power Sources*, 2009, **187**, 39–48.
4 M. Mirzaeian and P. J. Hall, *Electrochim. Acta*, 2009, **54**, 7444–7451.
5 C. Tran, X. Yang and D. Qu, *J. Power Sources*, 2010, **195**, 2057–2063.
6 F. H. B. Lima, M. L. Calegaro and E. A. Ticianelli, *Electrochim. Acta*, 2007, **52**, 3732–3738.
7 A. Débart, J. Bao, G. Armstrong and P. G. Bruce, *J. Power Sources*, 2007, **174**, 1177–1182.
8 J. Han, N. Li and T. Zhang, *J. Power Sources*, 2009, **193**, 885–889.
9 T. Wang, M. Kaempgen, P. Nopphawan, G. Wee, S. Mhaisalkar and M. Srinivasan, *J. Power Sources*, 2010, **195**, 4350–4355.
10 Y. Lu, Z. Xu, H. A. Gasteiger, S. Chen, K. Hamad-Schifferli and Y. Shao-Horn, *J. Am. Chem. Soc.*, 2010, **132**, 12170–12171.
11 Y. Li, J. Wang, X. Li, J. Liu, D. Geng, J. Yang, R. Li and X. Sun, *Electrochem. Commun.*, 2011, **13**, 668–672.
12 G. Q. Zhang, J. P. Zheng, R. Liang, C. Zhang, B. Wang, M. Au, M. Hendrickson and E. J. Plichta, *J. Electrochem. Soc.*, 2011, **158**, A822–A827.
13 F. Kong, *Electrochim. Acta*, 2012, **68**, 198–201.
14 J. Qiao, L. Xu, L. Ding, L. Zhang, R. Baker, X. Dai and J. Zhang, *Appl. Catal., B*, 2012, **125**, 197–205.
15 D. Pytches, *Electron. Power*, 1983, **29**, 577–580.
16 Zinc - Air Batteries - A Global Strategic Business Report, Global Industry Analysts, Inc.
17 K. M. Abraham and Z. Jiang, *J. Electrochem. Soc.*, 1996, **143**, 1–5.
18 A. Kraytsberg and Y. Ein-Eli, *J. Power Sources*, 2011, **196**, 886–893.
19 J. Christensen, P. Albertus, R. S. Sanchez-Carrera, T. Lohmann, B. Kozinsky, R. Liedtke, J. Ahmed and A. Kojic, *J. Electrochem. Soc.*, 2012, **159**, R1–R30.
20 R. Padbury and X. Zhang, *J. Power Sources*, 2011, **196**, 4436–4444.
21 G. Cohn, D. Starosvetsky, R. Hagiwara, D. D. Macdonald and Y. Ein-Eli, *Electrochem. Commun.*, 2009, **11**, 1916–1918.
22 G. Cohn and Y. Ein-Eli, *J. Power Sources*, 2010, **195**, 4963–4970.
23 G. Cohn, D. D. Macdonald and Y. Ein-Eli, *ChemSusChem*, 2011, **4**, 1124–1129.
24 P. Jakes, G. Cohn, Y. Ein-Eli, F. Scheiba, H. Ehrenberg and R. Eichel, *ChemSusChem*, 2012, **5**, 2278–2285.
25 B. Shvartsev, H. Shasha, E. Gileadi, R. Eichel and Y. Ein-Eli, unpublished results, to be submitted.
26 F. C. Laman, M. W. Matsen and J. A. R. Stiles, *J. Electrochem. Soc.*, 1986, **133**, 2441–2446.
27 E. Karden, S. Buller and R. W. De Doncker, *J. Power Sources*, 2000, **85**, 72–78.
28 M. Eswaran, N. Munichandraiah and L. G. Scanlon, *Electrochem. Solid-State Lett.*, 2010, **13**, A121–A124.
29 M. Mirzaeian and P. J. Hall, *J. Power Sources*, 2010, **195**, 6817–6824.
30 H. Arai, S. Miiller and O. Haas, *J. Electrochem. Soc.*, 2000, **147**, 3584–3591.
31 X.-H. Yang and Y.-Y. Xia, *J. Solid State Electrochem.*, 2010, **14**, 109–114.
32 O. Raz, D. Starosvetsky, T. Tsuda, T. Nohira, R. Hagiwara and Y. Ein-Eli, *Electrochem. Solid-State Lett.*, 2007, **10**, D25–D28.
33 O. Raz, Z. Shmueli, R. Hagiwara and Y. Ein-Eli, *J. Electrochem. Soc.*, 2010, **157**, H281–H286.
34 W. Shen, M. Tomkiewicz and C. Lévy-Clément, *J. Appl. Phys.*, 1994, **76**, 3635–3639.
35 C. Tran, J. Kafle, X. Yang and D. Qu, *Carbon*, 2011, **49**, 1266–1271.
36 P. E. Laibinis, C. E. Stanton and N. S. Lewis, *J. Phys. Chem.*, 1994, **98**, 8765–8774.
37 A. J. Nozik and R. Memming, *J. Phys. Chem.*, 1996, **100**, 13061–13078.
38 C. H. Hsu and F. Mansfeld, *Corrosion*, 2001, **57**, 747–748.
39 P. Schmuki, H. Bohni and J. A. Bardwell, *J. Electrochem. Soc.*, 1995, **142**, 1705–1712.
40 H. Jung, J. Hassoun, J. Park, Y. Sun and B. Scrosati, *Nat. Chem.*, 2012, **4**, 579–585.
41 P. Albertus, G. Girishkumar, B. McCloskey, R. S. Sánchez-Carrera, B. Kozinsky, J. Christensen and A. C. Luntz, *J. Electrochem. Soc.*, 2011, **158**, A343–A351.
42 Y. Shao, S. Park, J. Xiao, J.-G. Zhang, Y. Wang and J. Liu, *ACS Catal.*, 2012, **2**, 844–857.
43 Y. Gao, C. Wang, W. Pu, Z. Liu, C. Deng, P. Zhang and Z. Mao, *Int. J. Hydrogen Energy*, 2012, **37**, 12725–12730.
44 Y. Wang, *Electrochim. Acta*, 2012, **75**, 239–246.